Comprehensive Analysis Modeling of Small-Scale UAS Rotors

Carl R. Russell
Research Engineer
NASA Ames Research Center
Moffett Field, CA, USA

Martin K. Sekula
Research Engineer
NASA Langley Research Center
Hampton, VA, USA

ABSTRACT

Multicopter unmanned aircraft systems (UAS), or drones, have experienced explosive sales volume and application growth in recent years. With this growth comes demand for increased performance as the limits of existing technologies are reached. In order to improve the design of multicopter UAS aircraft, better validated performance prediction tools are needed. This paper presents the results of a study aimed at using the rotorcraft comprehensive analysis code CAMRAD II to model a multicopter UAS rotor in hover. Parametric studies were performed to determine the level of fidelity needed in the analysis code inputs to achieve results that match test data. Overall, the results show that CAMRAD II is well suited to model small-scale UAS rotors in hover. This paper presents the results of the parametric studies as well as recommendations for the application of comprehensive analysis codes to multicopter UAS rotors.

INTRODUCTION

The recent proliferation of multicopter unmanned aircraft systems (UAS), or drones, has begun to generate interest within the research community into the aerodynamic performance of these types of aircraft. The airframes of multicopter UAS designed and built thus far have largely been generated using iterative "cut and try" type methods; however, the limitations of these iterative design methods are starting to become apparent. UAS end-users often desire higher performance compared to the capabilities of many drones available today, particularly with respect to endurance and range.

While improved battery capacity and increased efficiency of electrical components such as motors and electronic speed controllers will certainly improve future UAS performance, vehicles will also need to be better designed for optimum aerodynamic performance. One way to accelerate the development of these optimized designs is to apply software tools to better predict rotor and airframe performance. Multiple recent studies have focused on the application of computational fluid dynamics (CFD) tools at the multicopter UAS vehicle scale [Refs. 1 and 2]. Others have focused on using various helicopter inflow models to predict performance [Ref. 3]. The study described here focuses on using the helicopter comprehensive analysis tool CAMRAD II [Ref. 4].

Presented at the AHS International 73rd Annual Forum & Technology Display, Fort Worth, Texas, USA, May 9-11, 2017.

Various parametric studies were performed as part of this research effort in order to determine the level of fidelity needed to accurately predict UAS rotor performance. The primary focus of this paper is on hover performance predictions for the T-Motor 15x5 propeller [Ref. 5] used on the Straight Up Imaging (SUI) Endurance [Ref. 6]. This vehicle and propeller were chosen because data collected in a previous study [Ref. 7] were readily available for validation.

Results are presented in the subsequent sections showing the effects of several different variations on the CAMRAD II inputs. Airfoil aerodynamic properties were generated using both a panel code and a Navier-Stokes CFD code. Variations on the number of airfoil tables used to describe the blade sectional aerodynamics were explored. The different inflow models employed by CAMRAD II were also tested, and finally, the rotor blade structural model was exercised to determine whether it had a significant impact on rotor performance predictions. The Conclusions section of this paper will give recommendations based on the results presented here.

METHODOLOGY

The following sections present the different parametric studies that were carried out on the UAS rotor blades. First, a brief description is given of the experiment used to generate the validation data. This section is followed by a description of the analytical models of the rotor blades that were developed. Finally, the parametric studies of blade sectional aerodynamics, various inflow models, and structural modeling effects will be presented.

Experimental Setup

Experimental data were acquired for the SUI Endurance rotor as part of a larger test campaign described in Ref. 7, and the test hardware is briefly described here. The test setup used to acquire hover data for the isolated SUI Endurance rotor is shown in Fig. 1. While the photo shows the rotor installed in a wind tunnel, the hover data were, in fact, collected in a lab, where the closest wall was approximately 30 feet away. The effect of air recirculation on the performance measurements was therefore very minimal.

Forces and moments were acquired using a six-axis load cell; however, for the isolated rotor in hover, only the thrust and torque are of any real interest. Power was provided to the motor via a DC power supply to avoid complications associated with batteries. The rotor speed was controlled with a wired servo controller operating over a USB interface. This setup allowed for finer control of rotor RPM than would be possible with a radio controller typically used for this type of rotor, and also alleviated the possibility of any radio interference with the load cell instrumentation. Rotor speed was varied in increments of 500 RPM through the typical operating range of this rotor (2,000 to 4,500 RPM), and data were recorded at each rotor speed. The thrust and torque for this rotor are plotted as a function of rotor RPM in Fig. 2.

Analytical Model

The analytical model of the SUI Endurance rotor, the T-Motor Carbon Fiber 15x5 (Fig. 3), was developed based on 3-dimensional scan of the blades. The blade geometry was surveyed using a Creaform laser scanning system and converted to a CAD model. Slices were taken at 22 radial stations, and the airfoil geometry, twist, and chord distribution were extracted. The extracted geometry is provided in Table 1. The Reynolds number is also given in Table 1 for the nominal rotor speed of 3,500 RPM. The airfoil cross-sections with chord lengths normalized to a value of 1 are presented in Fig. 4. The station-wise geometry was employed to develop both the structural and aerodynamic components of the analytical model.

Unlike traditional helicopter blades, which often only use one or two different airfoil shapes for their entire span, the SUI Endurance blades have a continuously varying airfoil section. This type of variation is typical for small-scale UAS blades, as their small size allows for the molding of arbitrary shapes. The modeling of the variation in blade cross section is discussed later. Another notable difference between the blades modeled here and a typical helicopter blade is the large blunt trailing edge in the airfoil, particularly at the blade tip. This trailing edge geometry is likely present due to manufacturing limitations at this small scale on mass-produced blades.

Figure 1. SUI Endurance isolated rotor hover test configuration.

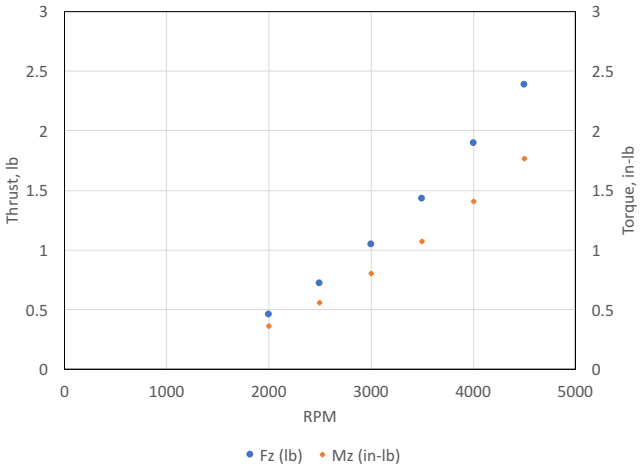

Figure 2. SUI Endurance isolated rotor hover test results.

Figure 3. T-Motor Carbon Fiber 15x5 blades.

Table 1. SUI Endurance blade geometry distribution

Section	r (in)	r/R	theta (deg)	chord (in)	t/c (%)	Re
1	0.93	0.12	6.97	0.77	20.80	11,600
2	1.24	0.17	15.97	0.97	15.63	19,500
3	1.55	0.21	21.77	1.18	11.77	29,600
4	1.86	0.25	21.72	1.34	9.76	40,300
5	2.17	0.29	19.91	1.44	8.73	50,500
6	2.47	0.33	18.14	1.49	8.18	59,500
7	2.78	0.37	16.55	1.50	7.88	67,500
8	3.09	0.41	15.28	1.49	7.72	74,500
9	3.40	0.45	14.01	1.46	7.53	80,300
10	3.71	0.49	13.00	1.42	7.38	85,200
11	4.02	0.54	12.18	1.38	7.22	89,700
12	4.33	0.58	11.39	1.33	7.11	93,200
13	4.64	0.62	10.76	1.27	7.04	95,300
14	4.95	0.66	10.24	1.21	7.07	96,900
15	5.26	0.70	9.85	1.14	7.13	97,000
16	5.57	0.74	9.40	1.07	7.26	96,400
17	5.88	0.78	9.07	1.00	7.54	95,100
18	6.19	0.82	8.70	0.93	7.89	93,100
19	6.50	0.87	8.46	0.86	8.30	90,400
20	6.81	0.91	8.29	0.77	8.74	84,800
21	7.11	0.95	8.19	0.67	8.88	77,100
22	7.42	0.99	8.17	0.44	10.15	52,800

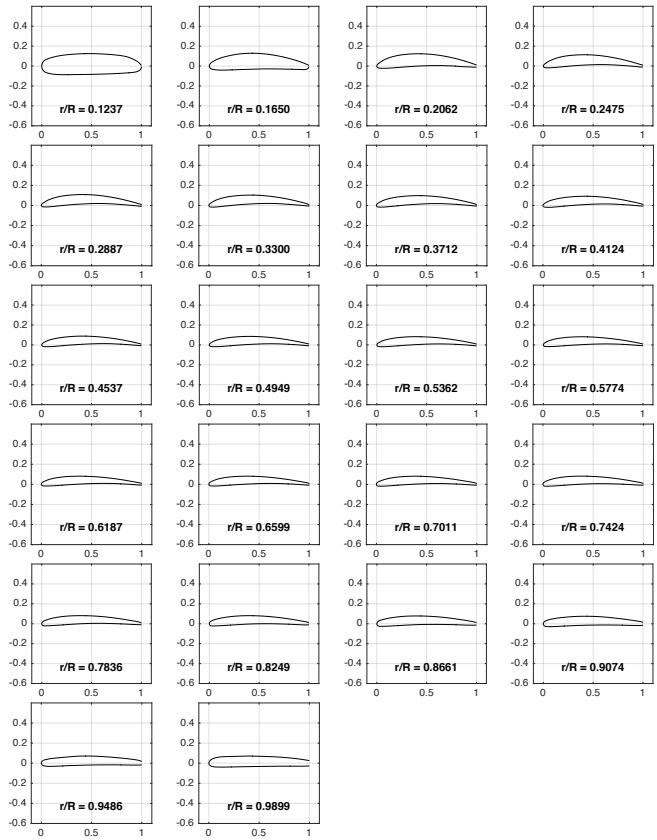

Figure 4. SUI Endurance airfoil geometry at various span-wise locations, chord length normalized.

Structural model

The elastic blade model contained in CAMRAD II was exercised to determine the impact of blade flexibility on the rotor performance. Certainly, if the blade can be modeled as a rigid beam, the development of the comprehensive analysis input deck can be significantly simplified. Blade deflections were measured using stereo-photogrammetry for both an SUI Endurance blade and a DJI Phantom 3 blade. The distinction between the two is significant, because while the SUI Endurance blade is constructed from carbon fiber over a wood core, the Phantom 3 blade is made from a much more flexible injection molded plastic. The results and process for measuring the deflections of the two rotors are described in Ref. 8.

The elastic blade model inputs were developed based on the laser-scanned geometries described in the previous section. The elastic and mass properties of the DJI Phantom 3 blade were determined experimentally through coupon testing, described in Ref. 8. For the SUI Endurance blade, mass and material properties were not available. The effects of the elastic blade were therefore approximated by iteratively adjusting the mass and elastic properties of the blades in the CAMRAD II input until the modeled deflection matched the experimentally determined blade deflection. In the case of the SUI Endurance blade, both the torsional and out-of-plane measured deflections were very small. The torsion deflection was unmeasurable, and the out-of-plane deflection was just over 1 mm at maximum thrust. The CAMRAD II results showed no significant difference in thrust or power when these deflections were included.

The DJI Phantom 3 rotor is much more flexible and presents a more interesting application of the elastic blade model; therefore, its results are described here in more detail. On the first attempt at applying the elastic blade model with the Phantom 3 rotor, the modeled out-of-plane deflection was approximately half of the observed deflection, and the torsional deflection was not captured at all. Because the primary interest was in determining the effect of elastic blade deflection on overall thrust and power, the material and mass properties were again iteratively adjusted, and an artificial moment was applied at the blade tip to induce the observed deflections. The resulting tip deflections are compared with the experimental results in Figs. 5 and 6.

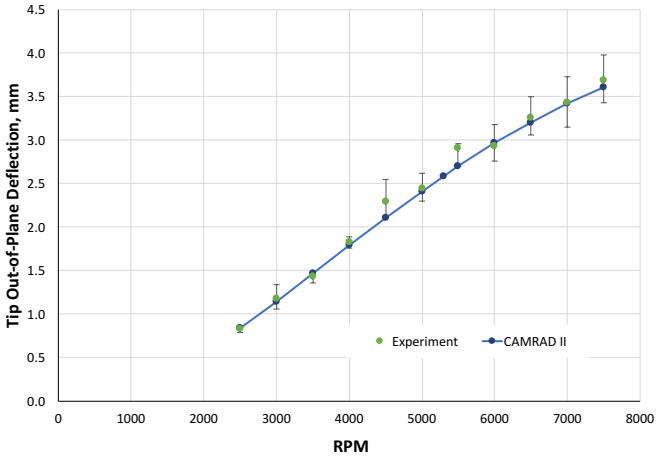

Figure 5. DJI Phantom 3 rotor out-of-plane tip deflection.

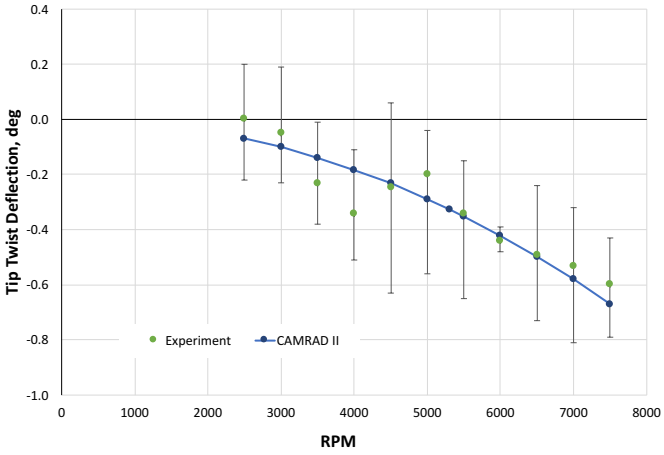

Figure 6. DJI Phantom 3 rotor torsional tip deflection.

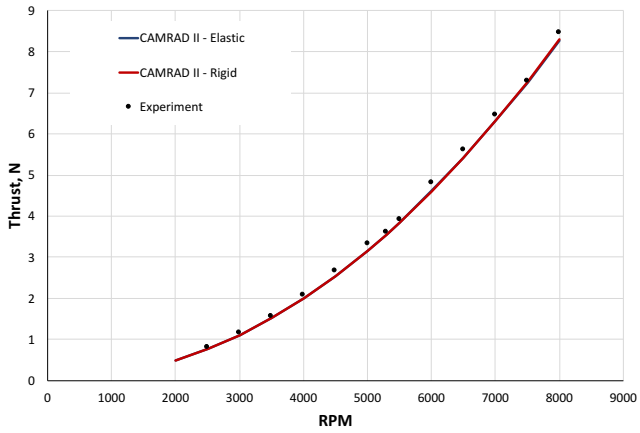

Figure 7. Predicted thrust for DJI Phantom 3 rotor.

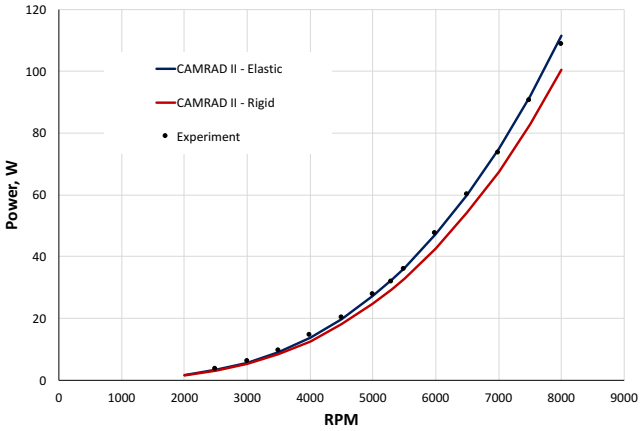

Figure 8. Predicted power for DJI Phantom 3 rotor.

Five different Phantom 3 blades were tested to generate the experimental results, and the error bars represent the upper and lower bounds on the measured deflections.

As shown above, with the modified inputs, the modeled blade deflections are within the bounds of the observed deflections. The effects of the elastic blade model on rotor thrust and power are shown in Figs. 7 and 8, respectively. In Figs. 5 through 8, the collective has been modified in order to better match the thrust at 5,300 RPM, the baseline thrust for the Phantom 3. All of the data points shown then use the same value for collective. As shown in Fig. 7, the elastic blade model has an insignificant effect on the thrust. In Fig. 8, however, using a rigid blade model causes the power to be under-predicted by approximately 10 percent.

The above analysis of the elastic blade model suggests that for carbon fiber blades at the scale discussed here, the elastic blade model can be ignored without any significant effect on rotor performance predictions. For the injection molded plastic blades, modeling blade deflection is important, particularly in predicting rotor power. A modified approach is needed to accurately predict the blade deflections, as the above deflections were obtained artificially. If the comprehensive analysis is being used to predict the performance of a yet-to-be manufactured blade, experimental data will not be available to validate the results.

Aerodynamic Model

CAMRAD II can utilize several different methodologies to model the aerodynamic loads on rotor blades. These methods span a large range of fidelity. Airfoil aerodynamic coefficients can be approximated using linear equations or spanwise-varying multi-dimensional airfoil tables. Likewise, the rotor flow field models can vary in complexity from simple linear inflow approximations to multi-trailer deforming wake models to coupled CFD analyses. The present model employs a set of 2-dimensional airfoil coefficient tables for determining the local lift, drag, and pitching moment coefficients. These tables, conforming to the C81 airfoil table format, were developed using software which utilized two aerodynamic solvers, XFOIL and

FUN3D [Refs. 9 and 10], to determine the airfoil coefficients.

Airfoil analysis

In-house software was developed to create C81 airfoil tables using an existing NACA-0012 table as a template. This tool would then substitute analytically-determined aerodynamic coefficients for all combinations of angle of attack and Mach number within a user-specified range – for this analysis, Mach numbers were limited to less than 0.5, and the angle of attack range was determined based on the fidelity of the analytical tool employed to calculate the aerodynamic coefficients. The Reynolds number for each airfoil was adjusted not only for changes in Mach number, but also to account for the large variation in the blade chord (see Table 1). Based on these combination of chord lengths and Mach number range, the airfoil Reynold numbers at the conditions analyzed were less than approximately 400,000.

CFD Analysis

The FUN3D computational fluid dynamics analysis was employed to determine 2-dimensional airfoil coefficients. The analysis utilized a triangular mesh extending 30 chord lengths around the airfoil with a minimum spacing set such that the y+ values were less than one across the range of Reynolds numbers analyzed. The grid for each airfoil consisted of approximately 70,000 nodes. For each flow condition examined with FUN3D, a steady solution was first calculated. Then the lift coefficient iteration record was examined to determine if an unsteady, time-accurate second order analysis was required. This decision was based on a de-trended standard deviation calculation of the last 10 percent of the iteration record. If the convergence criteria are not met, then the analysis is restarted using a time-accurate solution. For both the steady and time-accurate solutions, the stopping tolerance was set to 10^{-12}, and maximum number of iterations was 2500 and 4000 (with 50 sub iterations), respectively. The time-accurate analysis employed an A-S turbulence mode. The range of angles of attack was from -15 to +15 degrees in order to produce airfoil tables usable for both hover and forward flight.

Panel Method Analysis

Airfoil tables were also generated using XFOIL v6.9 analysis. XFOIL is a panel-method analysis whose formulation includes an approximation of viscosity effects. The default number of 20 iterations for converging the viscous solution is employed in the present analysis. The angle of attack range examined by this analysis is more limited than FUN3D's, from -5 to 9 degrees. This smaller range is required to minimize convergence issues.

The main inputs into both aerodynamic analyses consisted of airfoil coordinates, Reynolds number, and Mach number. The primary outputs were lift, drag, and pitching moment coefficients for each Mach-angle of attack combination. Two sets of sample lift and drag coefficient pitch polars for SUI Endurance rotors are presented in Figs. 9 and 10. These figures compare lift and drag coefficients for the NACA-0012 airfoil and ones calculated using XFOIL and FUN3D for T-Motor airfoils located 66% and 91% radial stations at a Mach number of 0.2. NACA-0012 coefficients are represented by circle symbols, while FUN3D coefficients are denoted by blue lines and XFOIL coefficients by red lines.

These figures demonstrate the capabilities and limitations of these analyses. The airfoil analyzed in Fig. 9 (airfoil profile for r/R=0.66 in Fig. 4) is highly cambered as evident from the large offset at 0 degree angle of attack. Both XFOIL and FUN3D depict this trait and generally match the lift-curve slope for this airfoil. On the other hand, XFOIL struggles to converge to a solution at negative angles of attack (as evident by the large change in the lift coefficient and a spike in the drag coefficient). For positive angles of attack, drag predictions from both analyses follow the trend, although XFOIL appears to predict lower drag coefficient values compared to FUN3D.

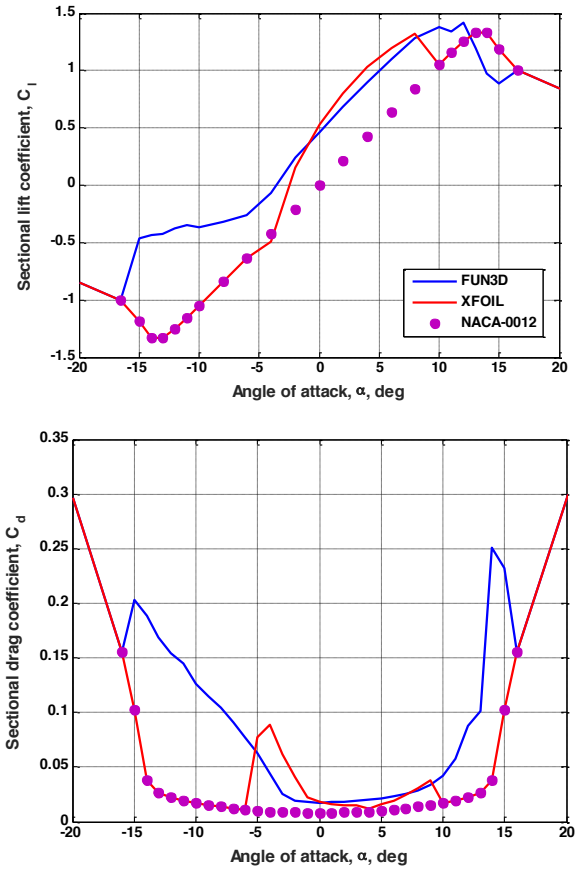

Figure 9. SUI Endurance airfoil coefficients, r/R = 0.66, M = 0.2.

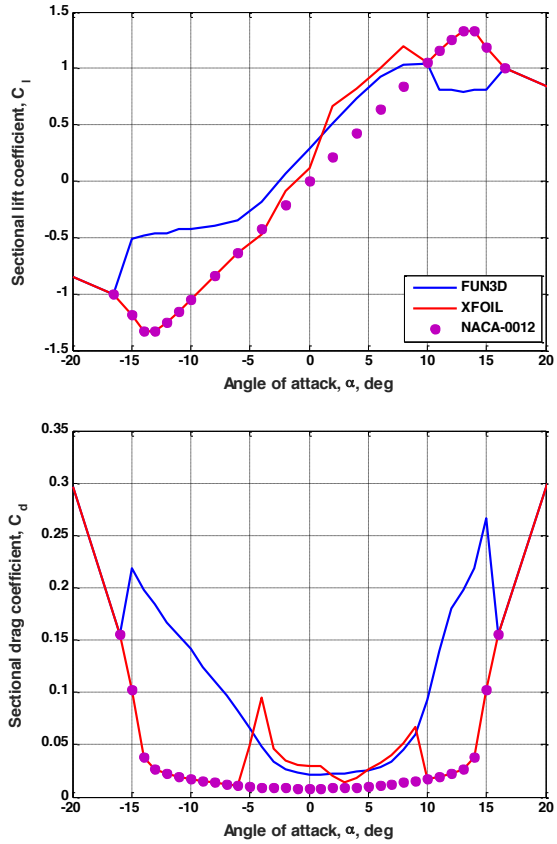

Figure 10. SUI Endurance airfoil coefficients, r/R = 0.91, M = 0.2.

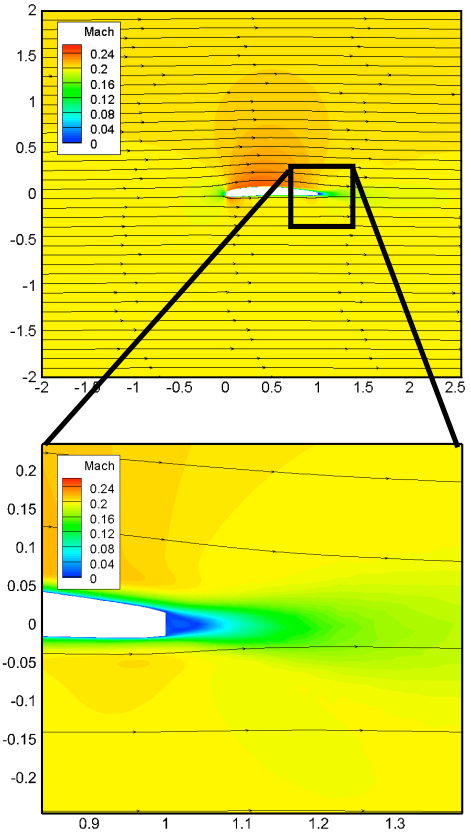

Figure 11. SUI Endurance airfoil 2-D velocity profile, FUN3D, r/R = 0.91, M = 0.2.

Similar observations can be made for the airfoil predictions at r/R=0.91, presented in Fig. 10. XFOIL-determined coefficients indicate that the analysis tool is not converging to a solution even at low, positive angles of attack. This convergence problem may be associated with the aerodynamic environment arising from the blunt trailing edge of this airfoil (see Fig. 4). The trailing edge separated flow region is clearly visible in Fig. 11, which presents the 2-dimensional aerodynamic environment (M = 0.2, α = 0°) for this airfoil.

The large blunt trailing edge noted in the airfoils near the blade tip is due to a combination of manufacturing limitations and scale. The chord near the blade tip is small, approximately 11 mm, at 0.99R. There is a physical limitation on how thin the trailing edge of an airfoil can be fabricated before it becomes too delicate. As the airfoil chord decreases, the thickness of the airfoil does as well. One exception is the trailing edge of the airfoil. Once the scale is small enough that the manufacturing limitations come into play, the trailing edge thickness can become comparable to the maximum thickness of the airfoil. This issue is most clearly visible in Fig. 4, r/R = 0.99.

The airfoil coefficients presented in Figs. 9 and 10 indicate that XFOIL is an adequate tool to generate airfoil tables within the linear range of the lift curve. This limitation on angle of attack constrains the utility of the XFOIL-produced airfoil tables to hover and low advance ratio edgewise flight. Likewise, the scale of the physical blades used to measure the airfoil geometry needs to be considered when determining if XFOIL is an adequate analytical tool, particularly when a large blunt trailing edge is present.

Rotor Performance Sensitivity to Airfoil Analysis

Rotor performance was calculated using CAMRAD II to determine the effect of the airfoil analysis on rotor thrust and power. For convenience, the structural model was assumed to be rigid. Furthermore, in order to maintain model-to-model consistency, the various modeling parameters in the aerodynamic models were set to their default values for hover flight. For this study, the free wake aerodynamic model was employed. Since CAMRAD II is limited to 20 spanwise airfoil definitions, only the outboardmost 20 of the 22 airfoil tables were utilized. A sensitivity study was conducted (not presented) which indicated that the inboard

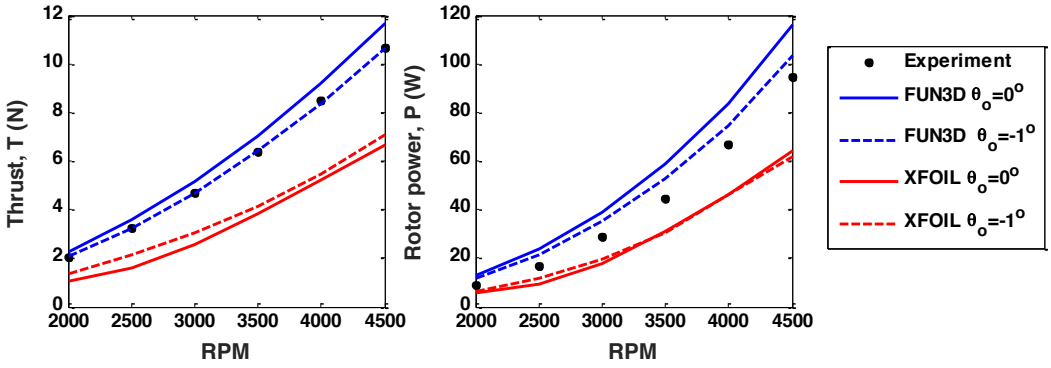

Figure 12. Effect of airfoil analysis on SUI rotor performance, free wake, hover.

airfoil tables did not affect the rotor thrust and power – an expected result due to the low dynamic pressure and short moment arm to the center of rotation.

The effect of airfoil analysis on rotor performance is provided in Fig. 12. In this figure, experimental thrust and power are compared to CAMRAD II models which incorporated FUN3D-developed and XFOIL-developed airfoil tables. The analysis using the FUN3D-developed airfoil tables overpredicts both the thrust and the power compared to the experimental data. The analysis using XFOIL-developed airfoil tables underpredicts both the power and thrust. This underprediction is associated with the incorrect lift and drag coefficient calculation at low angles of attack in XFOIL (see Figs. 9 and 10 for example). The angles of attack across most of the blade range between 2 and 3 degrees (not presented), which spans the angle boundary where XFOIL provides poor predictions. The effect of this issue is demonstrated in Fig. 12, where a -1 degree blade pitch index adjustment should reduce both thrust and power. This trend is present in the FUN3D-derived airfoil model, but does not occur in the XFOIL-derived model, even though CAMRAD II solution is numerically converged.

Inflow Modeling

The effect of the inflow model fidelity on rotor performance predictions was examined using the 20-airfoil model, whose airfoil tables were developed using FUN3D. CAMRAD II has three built-in wake models: uniform inflow, nonuniform inflow with a prescribed wake, and nonuniform inflow with a free wake. For brevity, the latter two will be refered to as prescribed wake and free wake, respectively. An RPM sweep, matching experimental RPM, was conducted using each of the three inflow models. Each inflow model was set up using its respective default hover settings.

Although the SUI Endurance rotor does not have a pitch bearing, the CAMRAD model included a pitch bearing near the root (0.05R) in order to allow changes in the blade indexing through the use of a collective pitch control. Three scenarios were examined during the couse of this study: 1) the pitch index set to zero to closely match the blade pitch to the actual scanned rotor geometry; 2) adjust the pitch index to match the experimental thrust; and 3) adjust the pitch index to match the experimental power. For the latter two cases, the pitch index adjustment was performed manually in one degree increments until the analytical curve qualitatively matched the experimental data – the pitch index was not adjusted as a function of RPM.

A comparison of the experimental data to the analytical performance curves developed using the three inflow models is presented in Fig. 13. The three sets of analyses were conducted with the pitch index set to zero degrees. All three models overpredict the thrust and power. The uniform inflow and free wake analyses match thrust and power very closly to one another, while the prescribed wake results in higher thrust and slightly higher power than the other two inflow models.

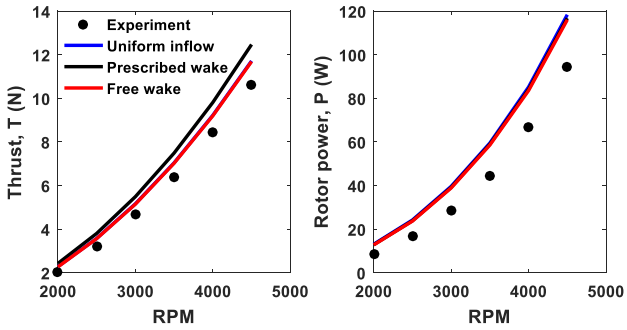

Figure 13. Effect of wake modeling on SUI performance, $\theta_o = 0^o$, hover.

Further insight can be gleaned by examining the spanwise distribution of some of the aerodynamic parameters of the blades. These parameters, for the 4500 RPM case, are presented in Fig. 14. The local angle of attack distribution is presented in Fig. 14a. The prescribed wake model generally exhibits the highest angles of attack across the entire blade, which coincides with the higher thrust predictions compared to the other two models. The free wake model generally

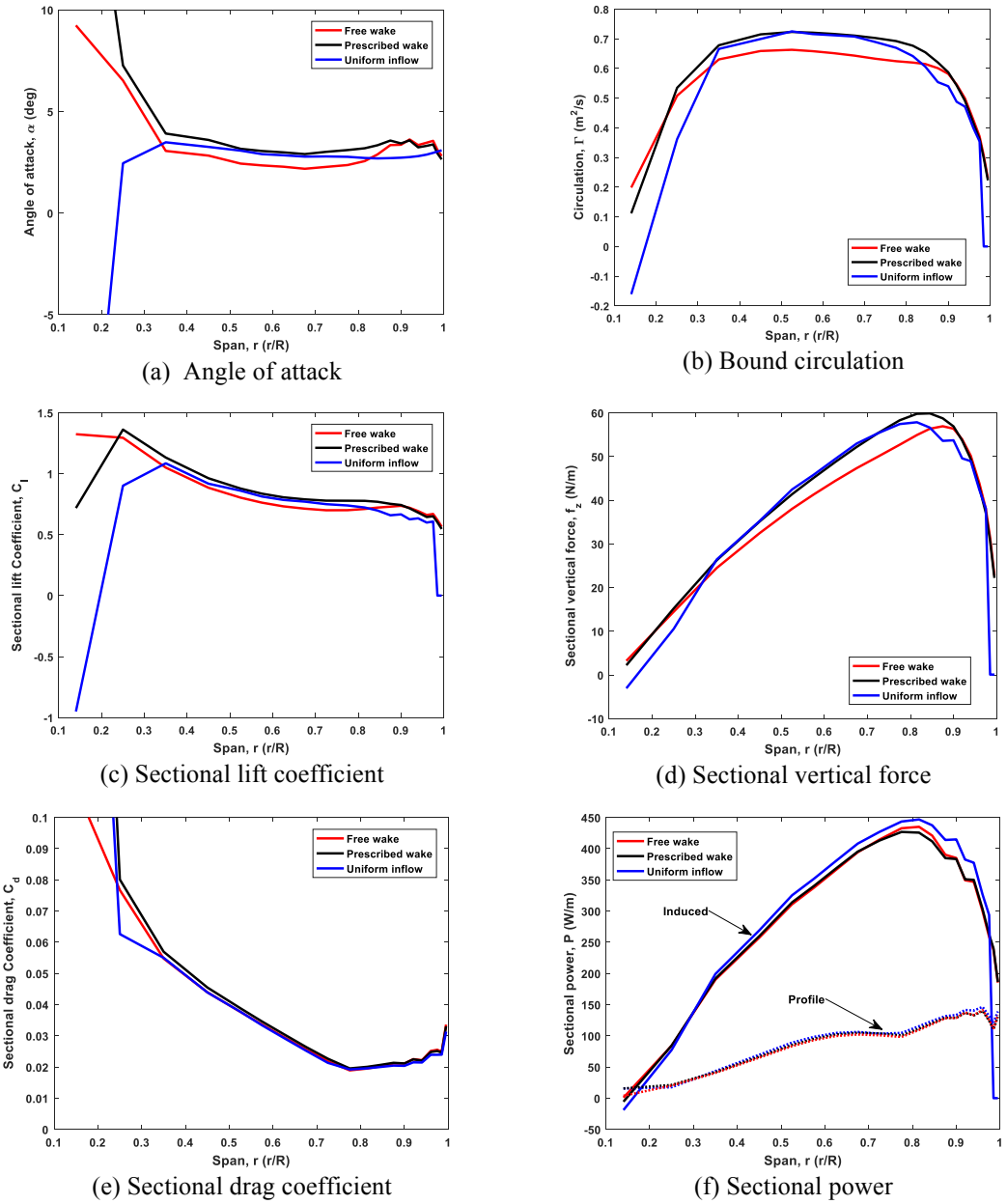

Figure 14. Effect of wake models on the spanwise distribution of aerodynamic parameters, θ_o = 0°, 4500 RPM, hover, FUN3D airfoil tables.

follows the same general angle of attack trends as the prescribed wake model, but with approximately a negative one degree offset. One exception to this offset is near the blade tip, where both model closely match each other with a slight increase in the angle of attack. More than likely, this blade tip similitude is caused by the proximity of the tip vortex. This conjecture is supported by the results of the uniform inflow model, which lacks a tip vortex model and does not exhibit the same trend near the blade tip. Furthermore, the uniform inflow model indicates a large decrease in the angle of attack near the blade root. The general differences in angles of attack can be related to the distribution of bound circulation across the rotor blades (Fig. 14b). The free wake model has a lower level of vorticity across the majority of the rotor blade, thereby a lower induced velocity in the perpendicular direction, which affects the angle of attack. Not surprisingly, the lift coefficient distribution (Fig. 14c) follows a similar trend to the angle of attack. The lift distribution, a combination of the lift coefficents with the local dynamic pressure, (Fig. 14d) indicates that the higher inboard angles of attack produced by the prescribed wake tend to shift the center of lift more inboard than the free wake model, and the uniform inflow shifts the center of lift even further inboard.

The drag coefficent near the blade root (Fig. 14e) indicates large variations in values between the various inflow models. Further out on the blade, the drag coefficients follow similar trends, although there are small differences in the C_d due to inflow model choice. Of more sigificance in understanding the impact of the inflow models is the sectional power distribution presented in Fig. 14f. The total power is broken up into profile and induced power components. The free wake and prescribed wake models exhibit similar power distributions across the rotor blade. The sectional induced power for the uniform inflow model is significantly higher than that of the other two models, yet the total rotor power is approximately the same (see Fig. 13). This apparent discrepancy between sectional power and integrated rotor power is caused by a tip loss paramter, b_{tip}. This parameter provides a tip flow correction by eliminating the lift and induced drag outboard of a user prescribed radial station. The effect is that the increased induced power on the inboard portion of the blade is offset by the suppression of the blade tip induced power. Without this parameter, the rotor power is overpredicted compared to the other models (not presented).

For each wake model, the pitch index of the blades was adjusted in one degree increments until the thrust predictions qualitatively matched the expermental data. The results of these adjustements on the rotor performance predictions are presented in Fig. 15. The free wake and uniform inflow models required a -1 degree adjustment in the pitch index to match the experimental thrust, resulting in a more accurate prediction of the power than the unadjusted pitch index models. The prescribed wake model required a -2 degree pitch index adjustment to match the experimental thrust. This adjustment resulted in a close match to the experimental power as well.

A comparison of the spanwise distribution of several key variables affecting the performance predictions for the 4500 RPM case are presented in Fig. 16. The angle of attack distribution for the three inflow models is provided in Fig. 16a. The angles of attack for the free wake and prescribed wake models are almost identical for the majority of the blade span eventhough the prescribed wake model pitch index is a degree less than the free wake pitch index. This difference indicates that the free wake model results in a higher induced inflow velocity. Also there are differences in the angles of attack at the two extreme ends of the blades. Near the root, small changes in inflow can result in large changes in the angle of attack since the tangential velocity is low in hover. At the blade tip, the free wake model angle of attack is approximately 0.8 degree higher than that of the prescribed wake model. It should be noted that there is a -1 degree difference in the blade pitch between the prescribed and free wake cases, therefore the impact of inflow velocity on the angle of attack appears to be smaller than further inboard on the blade. The uniform inflow model angle of attacks are generally higher for the majority of the blade, except for the tip, where they don't see the angle of attack increase seen in the other two models. At the blade root, the angles of attack significantly drop and are even negative, as opposed to the other two models, indicating a higher inflow velocity than the other inflow models. The bound circulation, Fig. 16b, reflects these differences in the angles of attack, as does the sectional lift coefficient, Fig. 16c.

The sectional vertical force, f_z, presented in Fig. 16d, indicates that the main difference in the sectional loads contributing to the rotor thrust occur between 0.75R and 0.95R for the free wake and prescribed wake models. This difference in force can be seen in Fig. 15, where the prescribed wake model has a slightly lower rotor thrust than the free wake model. The uniform inflow model more closely matches the f_z force of the prescribed wake model in the 0.8 to 0.95R, but inboard of 0.8R the load is much higher than the other models. Once again this increase is offset by force reduction due to the tip loss correction dicussed previously.

The sectional drag coefficient, presented in Fig. 16e, does not vary significantly between the three models, but the difference in sectional rotor power, Fig. 16f, is significant. While the profile drag components match closely, the induced power component for the prescribed wake model is significantly lower than the free wake and the uniform inflow models. This decrease in induced power can be traced back to the previously discussed decrease in the inflow velocity compared to the free wake (and uniform inflow) model.

The pitch index of the analytical models was adjusted to also match the experimental power. The results of this study are presented in Fig. 17. For all three inflow models, the pitch index was set to -2 degrees in order to match the experimental power. This adjustment resulted in the free wake and uniform inflow models under-predicting the thrust. These trends in thrust and power predictions follow the trends noted in Fig. 13, since the only difference between the two sets of cases is a -2 degree pitch index offset in all the models.

An examination of the spanwise distribution of aerodynamic parameters on the blades, similar to the ones provided in Figs. 14 and 16, was conducted, but with the exceptions of changes in magnitudes of the various parameters, appeared identical to Fig. 14, and is therefore omitted for sake of brevity.

The above analysis indicates that neither the uniform inflow or free wake models correctly predict the thrust-to-power ratio – if the thrust is correct, the power is under-predicted. The prescribed wake model did correctly predict both the thrust and power simultaneously, but only if the blade pitch

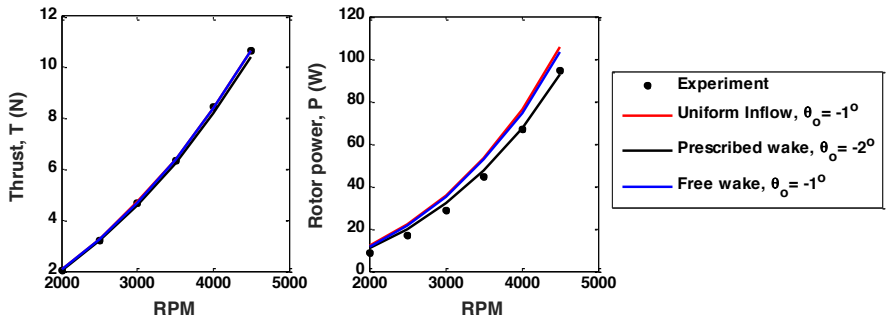

Figure 15. Effect of wake modeling on SUI performance, θ_o adjusted to match experimental thrust, hover.

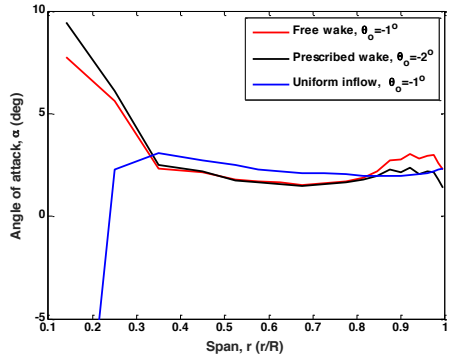

(a) Angle of attack

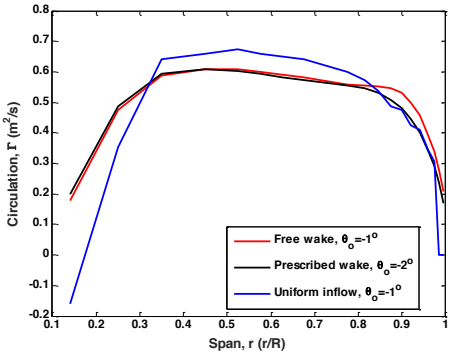

(b) Bound circulation

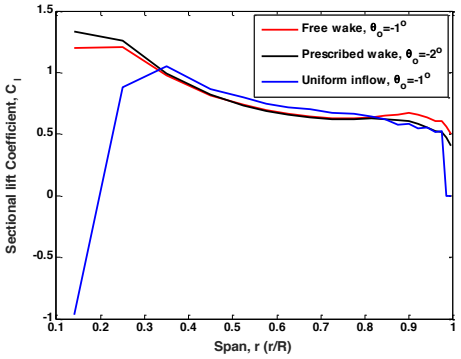

(c) Sectional lift coefficient

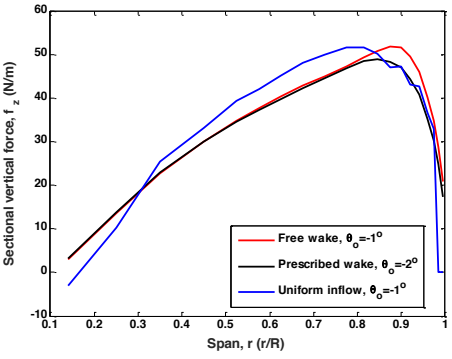

(d) Sectional vertical force

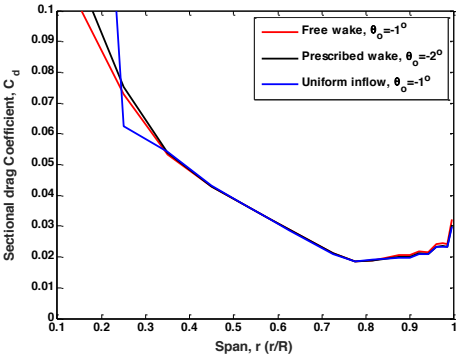

(e) Sectional drag coefficient

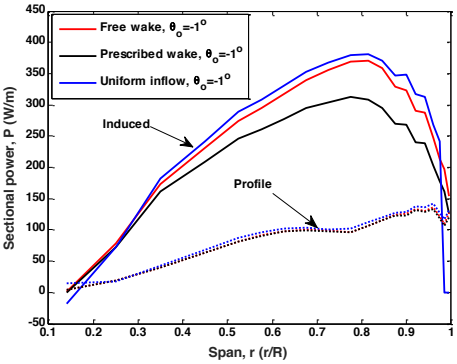

(f) Sectional power

Figure 16. Effect of wake models on the spanwise distribution of aerodynamic parameters, θ_o adjusted to match experimental thrust, 4500 RPM, hover, FUN3D airfoil tables.

index is adjusted. None of the models correctly predicted the thrust or power without a pitch index adjustment. The necessity of this adjustment indicates that one or more potential problems are present such as:

1. Incorrect induced inflow/circulation modeling
2. A systemic error in the blade scan used to develop model geometry (i.e. flawed airfoil contours, incorrect blade twist distribution, etc.)
3. Validity of the airfoil table

Inflow model discussion

The first of these issues was examined through a series of parametric studies where various CAMRAD II variables used to tune the inflow and wake models were systematically changed. This study was conducted with the free wake model using FUN3D-developed airfoil tables. The pitch index was set to 0 degrees. The variables included:

1. Tip vortex core radius
2. Inboard rolled-up trailed wake core radius
3. Free wake model formulation (Scully, Johnson, general method)
4. Tip vortex model type (single peak based on either maximum or outboard circulation, or a dual peak model)

These studies had a minor impact on thrust and even more limited on power. The only modeling variable that affected the performance was changing the root cutout. Increasing the size of the root cutout from 0.12R up to 0.3R was able to reduce the rotor thrust, but did provided only minor changes in rotor power.

Airfoil Distribution Sensitivity

The SUI Endurance rotor blades, like many other UAS rotor blades have a highly varying airfoil profile across the blade span. In order to provide the most accurate aerodynamic model, the preceding studies were conducted using airfoil tables developed for 20 blade stations. Depending on the range of angles of attack and Mach numbers, the number of conditions at which aerodynamic coefficients need to be determined to populate an airfoil table can be large. This large number of conditions may be numerically intensive if a CFD analysis is employed to generate the airfoil tables. Therefore it is of benefit to understand how sensitive UAS rotor performance is to the distribution and density of airfoil properties across the blade span.

An analysis was developed to systematically examine the sensitivity of rotor thrust and power to airfoil property distribution. The goal of the analysis is to define the minimum number of spanwise airfoil segments needed to properly model the rotor performance. The accuracy of the performance predictions is assessed by comparing the results of an RPM sweep conducted in CAMRAD II from 2,000 RPM to 4,500 RPM (in 500 RPM increments) to a baseline result. The metric employed in this study, *TR*, is the mean of the ratio of the thrust of the current model to the thrust of the baseline model:

$$TR = \frac{1}{n}\sum_{i=1}^{n}\left(\frac{T}{T_{bl}}\right)_i$$

Where T is the thrust of the current model at the i^{th} RPM case, T_{bl} is the baseline model thrust at the i^{th} RPM, and n is the number of cases in the RPM sweep.

The analysis starts with all 20 airfoil tables, the baseline model, and systematically replaces the inboard airfoil tables with the airfoil table from the next outboard station. The thrust and power are then calculated for the RPM sweep and the metric is recalculated to determine how the performance has changed. If the metric is within a user defined tolerance, ΔTR_{lim}, then all the inboard airfoil tables are replaced by the next outboard airfoil table. For example, after the analysis employing all 20 airfoil tables, the inboard-most airfoil table at station 0.21R would be replaced with the airfoil table for station 0.25R. In the next iteration, both airfoil tables at 0.21R and 0.25R would be replaced with the airfoil table for station 0.29R.

This process continues until the user-defined tolerance for the metric is exceeded, thereby signifying that the single airfoil region should not be extended to the current airfoil station. The last airfoil distribution not to exceed the

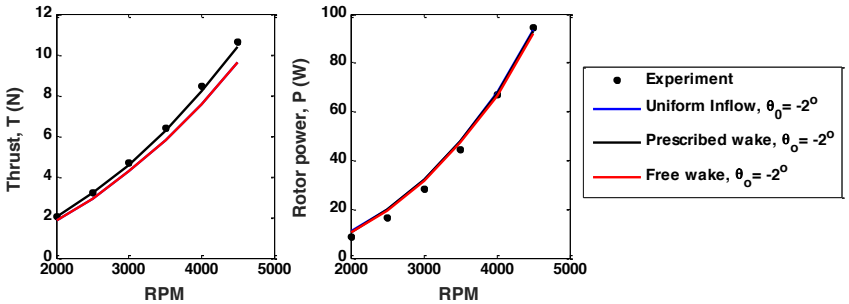

Figure 17. Effect of wake modeling on SUI performance, θ_o adjusted to match experimental power, hover.

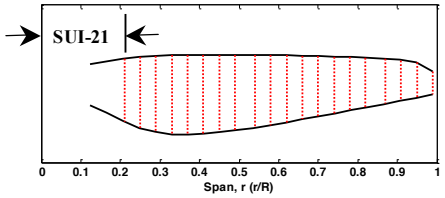

(a) Baseline, 1st segment.

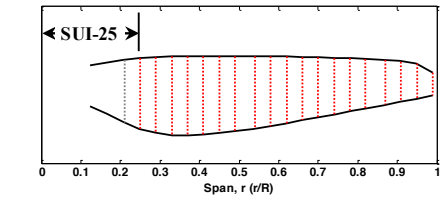

(b) 1st airfoil substitution, 1st segment.

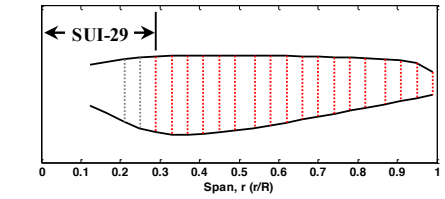

(c) 2nd airfoil substitution, 1st segment.

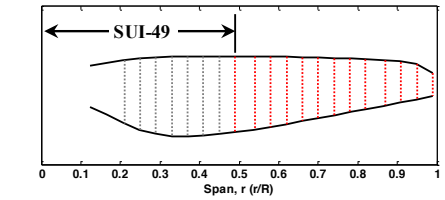

(d) 7th airfoil substitution, 1st segment.

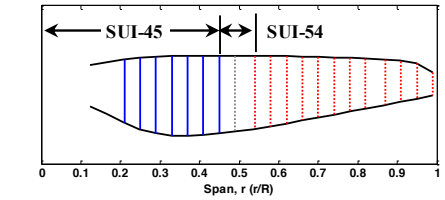

(e) 1st airfoil substitution, 2nd segment.

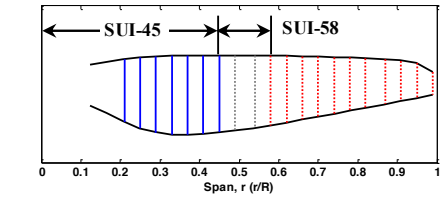

(f) 2nd airfoil substitution, 2nd segment.

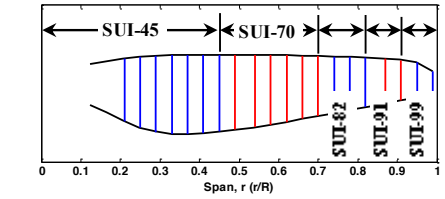

(g) Final airfoil distribution, 5 segments.

Figure 18. Graphical representation of the algorithm for the airfoil distribution study.

tolerance is designated as the new baseline and the process is restarted. In these subsequent restarts, the newly identified airfoil region is not affected by the airfoil replacement process. This process is continued until the tip of the blade is reached. A graphical representation of this algorithm is presented in Fig. 18.

Two analyses were performed, one where the metric tolerance, ΔTR_{lim}, was set to a maximum 1% change in the thrust compared to the baseline for each airfoil section, and a second case where the metric tolerance was set to 5%. Examining two different tolerance values provides an idea of how many airfoils are required to develop an analytical model capable of providing an adequate prediction of the rotor performance. Both cases were ran with a pitch index of -1 degrees.

The results of the airfoil segment-defining analysis for a maximum tolerance of 1% are provided in Fig. 19. This figure presents the impact of replacing inboard airfoil properties on the rotor thrust and power relative to the baseline thrust and power for each blade segment, T_{bl}* and P_{bl}*. (The asterisk signifies a segment baseline as opposed to the 20-airfoil model baseline.) To comply with the 1% limit on change in thrust within each blade segment, the analysis identified five blade segments: root to 0.49R, 0.49R to 0.70R, 0.70R to 0.82R, 0.82R to 0.91R, and 0.91R to the blade tip labeled Segments 1 through 5, respectively. Of note is that these segments become shorter further outboard as the dynamic pressure increases.

The thrust and power as a function of RPM for each intermediate step in the analysis where a new segment is identified is presented in Fig. 20. These are compared to the baseline, 20-airfoil model. The change in thrust and power with respect to the highest fidelity (baseline) model are both minimal, as expected since the airfoil segments were limited

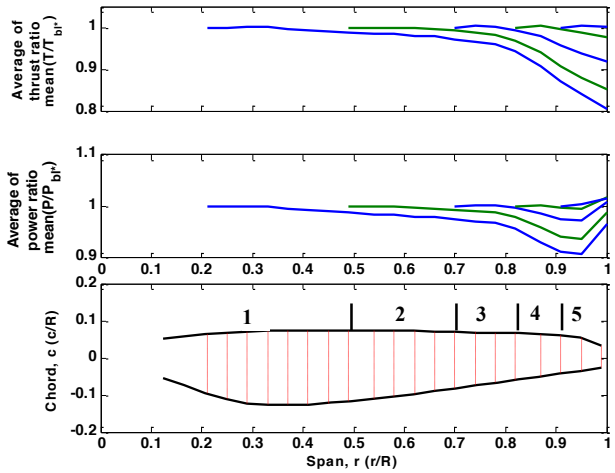

Figure 19. Change in thrust and power ratio due to changes in airfoil distribution, free wake, θ_o = -1 deg, ΔTR_{lim} = 0.01.

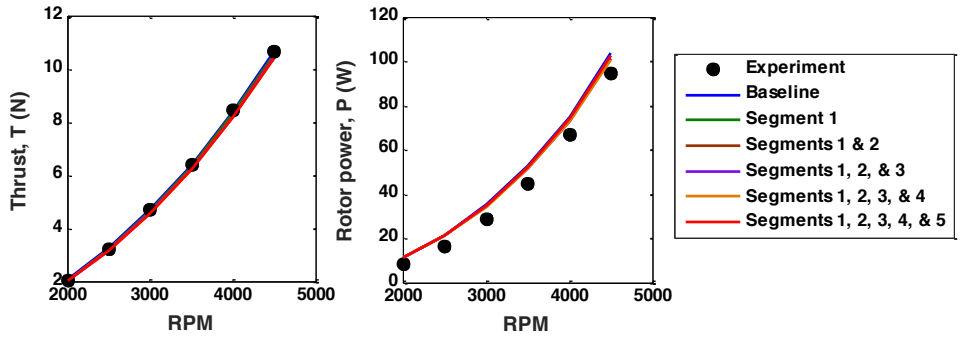

Figure 20. Effect of segment substitution on thrust and power, free wake, θ_o = -1 deg, ΔTR_{lim} = 0.01.

to a 1% maximum change in mean thrust compared to baseline. The thrust for the final, 5-segment model, is approximately 3 percent lower than the baseline, 20-segment model, regardless of RPM. The simplified model power is approximately 2 percent lower than the baseline across the RPM range.

The final simplified model reduced the number of airfoil properties across the blade from 20 to 5. The analysis assumed the outermost airfoil in each segment replaced all the inboard airfoils within that segment. This assumption raises the question of how sensitive the analytical model performance is to the choice of airfoil within each segment. Rotor performance analyses were conducted where the airfoil tables of each segment were systematically replaced by airfoils from the baseline model which fall within the span of the segment. For example, the inboardmost segment of the 5-segment model which spans from the root to 0.49R replaced seven airfoils from the detailed model with a single airfoil. By conducting an analysis of the rotor with each of these airfoils defining the segment aerodynamic properties, the sensitivity of rotor performance to the selection of airfoils for each segment can be determined.

The summary results of this study, examining the sensitivity of thrust and power to airfoil changes within each of the five segments, is presented in Fig. 21. This figure presents the mean thrust ratio and mean rotor power ratio (with respect to the 20-airfoil baseline) for each substituted airfoil. The thrust variation between the various airfoil substitutions is relatively small. The mean thrust ratio varies between 0.975 and 0.987. This small variation is expected since the analysis was geared towards maintaining accuracy in thrust predictions while minimizing the number of airfoils in the rotor model. The mean power ratio varies between 0.983 and 1.013 – a much larger range than the thrust ratio. The two segments that exhibited the largest variation in power were the inboardmost and the outboardmost segments, 1 and 5. The inboardmost segment represents the largest spanwise section of the blade and spans the section of the blade with the largest chord, but operates in the lowest dynamic pressure aerodynamic environment. The airfoil shape varies significantly within this segment (see Fig. 4), and may explain the difference in power. The outboardmost segment exhibits a one percent variation in power due to airfoil selection. The majority of this power variation comes from the use of the airfoil located at 0.99R. As discussed

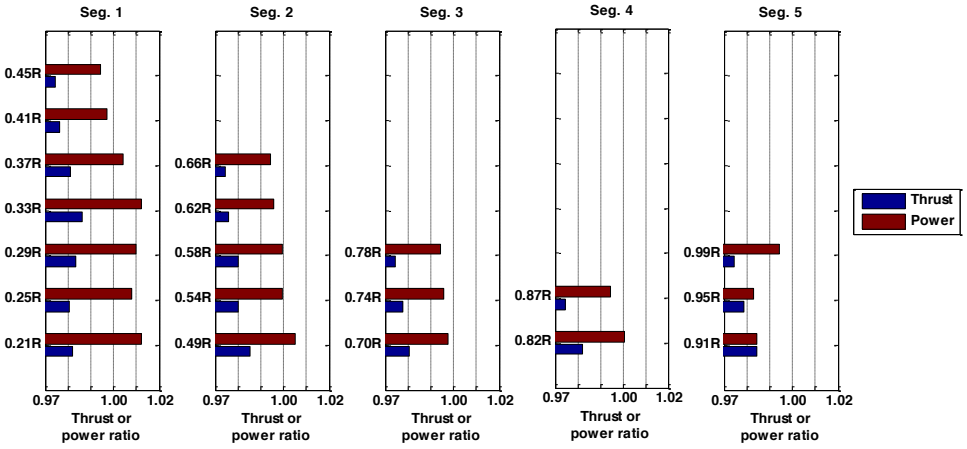

Figure 21. Effect of airfoil selection on thrust and power, free wake, θ_o = -1 deg, ΔTR_{lim} = 0.01.

previously, this airfoil has an extremely blunt trailing edge, resulting in high drag coefficients. Applying this airfoil to a large segment of the blade – in this case 9 percent – artificially raises the rotor power. Based on Fig. 21, the inboardmost and outboard most segments require more careful selection of airfoils. For the inboardmost segment, one should not select airfoils from near the blade root, while for the outboardmost segment, airfoils from near the blade tip should be avoided, especially if the airfoil exhibits the aforementioned blunt trailing edge.

The results of a second blade segment definition analysis are presented in Figs. 22 through 24. For this analysis the metric tolerance ΔTR_{lim} was set a maximum 5% change in the thrust compared to the baseline for each blade section. The results of the airfoil segment-defining analysis are provided in Fig. 22. The analysis determined that only two constant-airfoil blade segments are required to maintain the thrust variation within each segment to a maximum of 5%. These segments are defined from the blade root to 0.82R and 0.82R to the blade tip, utilizing airfoils from 0.78R and 0.99R. Using these two segments, the total thrust compared to the baseline, 20-airfoil model reduces approximately 7 percent while the rotor power reduces 5.5 percent, as shown in Fig. 23.

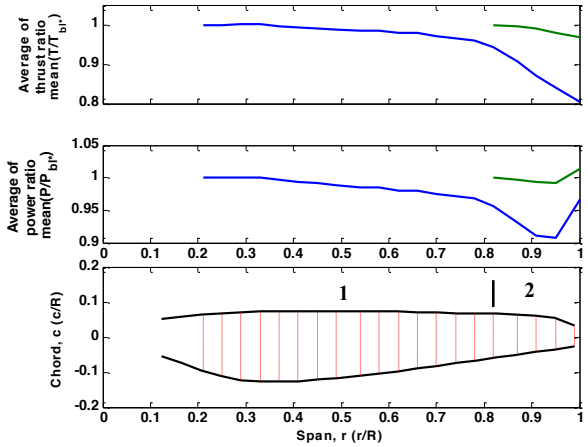

Figure 22. Change in thrust and power ratio due to changes in airfoil distribution, free wake, θ_o = -1 deg, ΔTR_{lim} = 0.05.

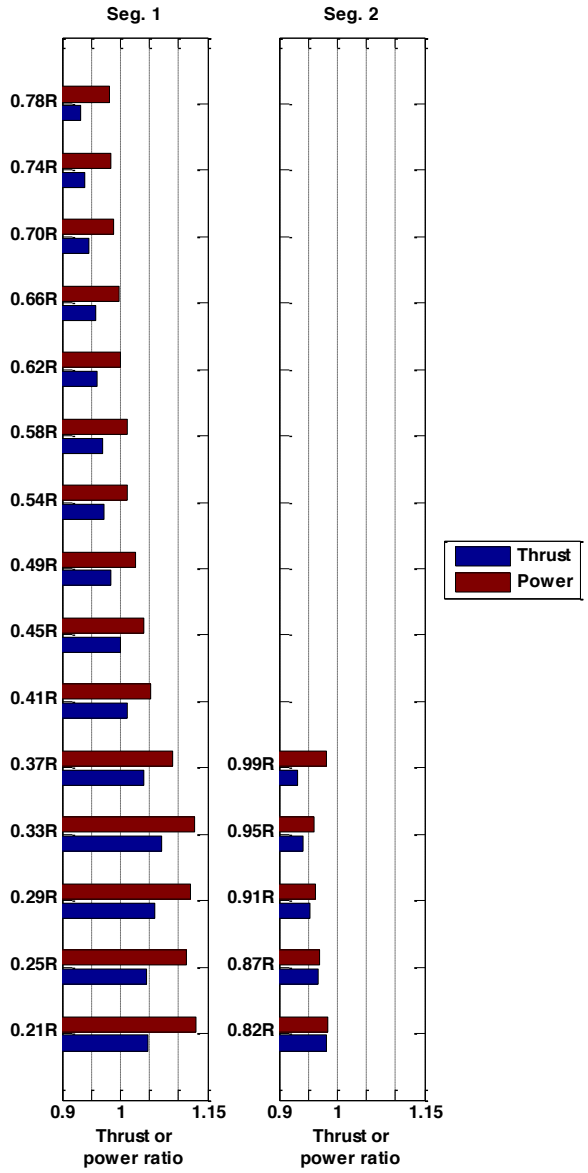

Figure 24. Effect of airfoil selection on thrust and power, free wake, θ_o = -1 deg, ΔTR_{lim} = 0.05.

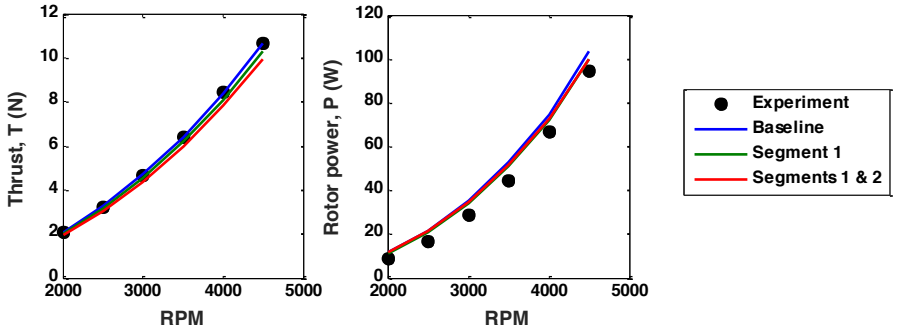

Figure 23. Effect of segment substitution on thrust and power, free wake, θ_o = -1 deg, ΔTR_{lim} = 0.05.

The effect of airfoil selection within each segment is presented in Fig. 24. The inboard segment spans approximately 80 percent of the blade and the choice of airfoil within this segment produces the largest variation in thrust and power, ranging from 0.93 to 1.07 for thrust and 0.98 to 1.13 for power. The inboardmost airfoils tended to result in overpredictions of the power and thrust due to their high camber. The outboard airfoils in this segment underpredicted the thrust, but resulted in correct power predictions compared to the 20-airfoil model. The outboard segment thrust varies from 0.93 to 0.98 compared to baseline, depending on the airfoil employed, and the power varies from 0.96 to 0.98 of baseline. Utilizing the outboardmost airfoil, 0.99R, results in the widest gap between thrust and power compared to the other four airfoils examined in this segment. Based on the impact of airfoil selection on thrust and power presented in Fig. 24, the choice of airfoil for the inboard segment should be from near the center of the segment, while the outboard segment airfoil should be selected from the more inboard airfoils, either 0.82R or 0.87R.

The effect of using a single airfoil table for defining the aerodynamic loads across the entire blade was also examined. The impact of the using various airfoils on the rotor thrust and power compared to the 20-airfoil model is presented in Fig. 25. The thrust can vary from approximately 80 to 120 percent of baseline while the power varies from 92 to 122 percent of baseline. The extreme values of these performance predictions were a result of using airfoils from near the root or tip of the blade. Utilizing airfoil tables from airfoils located on the blade section spanning 0.5 to 0.8R provided reasonable performance predictions within 5 percent of the baseline. This observation may not hold true for other UAS rotors since airfoil distributions may significantly vary from rotor to rotor.

CONCLUSIONS

The rotorcraft comprehensive analysis code CAMRAD II was used to conduct a series of parametric design studies to determine the level of modeling fidelity that is needed to model a multicopter UAS rotor in hover. Analytical models were developed based on 3-dimensional scans of UAS rotors. Airfoil tables used in CAMRAD II were developed using two methods, a computational fluid dynamics code, FUN3D, and a panel method code, XFOIL. Analytical performance predictions were compared to experimental data and trends between various fidelity analytical models were determined.

Overall, the results show that CAMRAD II is well suited to model small-scale UAS rotors in hover. In particular, the following observations have been made.

- Modeling of blade elasticity effects should be considered for rotors manufactured using methods such as injection molding using plastics or resins, since these rotors are more flexible than rotors made using composites. Rigid blade analytical models were demonstrated to underpredict the rotor power.
- Care must be used if applying a panel method analysis to determine airfoil aerodynamic coefficients. Such an analysis was found to be less accurate than a CFD analysis when analyzing airfoil geometries developed from scans of blade stations with small chord lengths. At these stations, manufacturing limitations can create a blunt trailing edge with a thickness comparable to the airfoil maximum thickness – a geometry which produces a large separated flow region.
- Regardless of the inflow model utilized in the analysis, the blade pitch index angle needed to be adjusted to match performance data as a function of RPM.
- Parametric studies of tip vortex models indicated a limited effect on performance predictions.

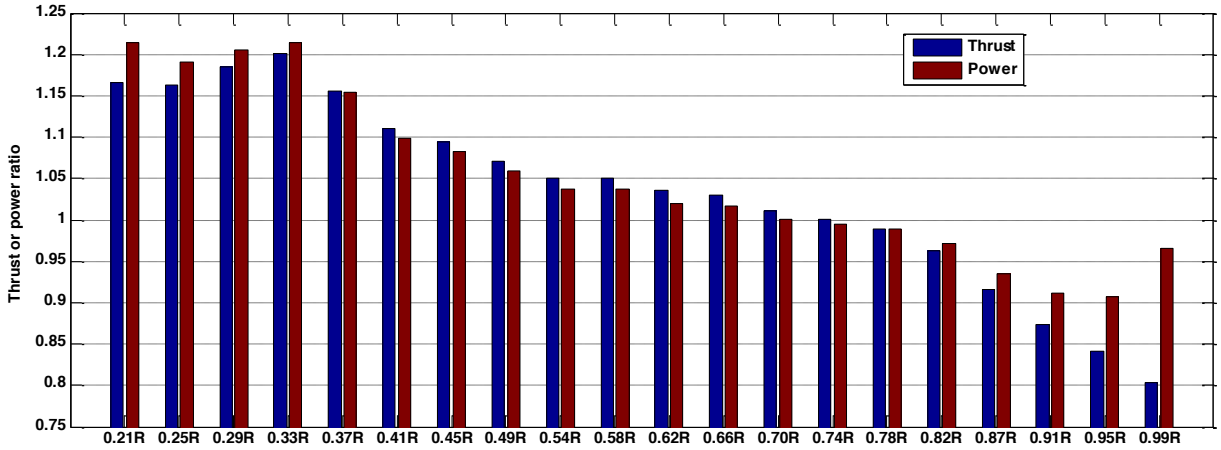

Figure 25. Effect of airfoil selection on thrust and power, one region, free wake, θ_o = -1 deg.

- Studies examining the effect of reducing the number of airfoils across the blade span indicated that reducing the number of airfoils across the blade span from 20 to 5 has a limited effect on the accuracy of rotor performance predictions. Reducing the number of airfoils to two introduces up to 7 percent differences in thrust, compared to the 20-airfoil baseline, and up to 12 percent difference in power. Using a single airfoil increases these differences to approximately 20 percent, depending on airfoil chosen. It was noted that a single airfoil model based on airfoils from blade stations ranging from 0.5 to 0.75R consistently provided performance predictions within 5 percent of baseline.

ACKNOWLEDGEMENTS

The authors would like to thank Eduardo Solis for providing the laser-scanned blade geometries. Nathalie Nowicki provided the measurements of elastic blade deflection. This work was supported by two NASA projects: the Design Environment for Novel Vertical Lift Vehicles (DELIVER) Sub-project, under the Convergent Aeronautics Solutions (CAS) Project; and the Revolutionary Vertical Lift Technology (RVLT) Project.

REFERENCES

1. Yoon, S., Ventura-Diaz, P., Boyd, D., Chan, W., and

2. Thibault, S., Holman, D., Trapani, G., and Garcia, S., "CFD Simulation of a Quad-Rotor UAV with Rotors in Motion Explicitly Modeled Using an LBM Approach with Adaptive Refinement," AIAA 55th Aerospace Sciences Meeting, Grapevine, TX, January 9-13, 2017.

3. Niemiec, R. and Gandhi, F., "Effects of Inflow Model on Simulated Aeromechanics of a Quadrotor Helicopter," American Helicopter Society 72nd Annual Forum, West Palm Beach, FL, May 16-19, 2016.

4. Johnson, W., "Technology Drivers in the Development of CAMRAD II," American Helicopter Society 3rd Decennial Aeromechanics Specialists' Meeting, San Francisco, CA, January 1994.

5. "Carbon Fiber Prop – T-Motor," http://www.rctigermotor.com/html/2013/prop_0805/16.html, accessed March 2, 2017.

6. "Products – Straight Up Imaging," http://www.straightupimaging.com/products/, accessed March 2, 2017.

7. Russell, C., Jung, J., Willink, G., Glasner, B., "Wind Tunnel and Hover Performance Test Results for Multicopter UAS Vehicles," American Helicopter Society 72nd Annual Forum, West Palm Beach, FL, May 16-19, 2016.

8. Nowicki, N., "Measurement and Modeling of Multicopter UAS Rotor Blade Deflection in Hover," Master's Thesis, KTH – Royal Institute of Technology, Stockholm, Sweden, July 2016.

9. Drela, M., "XFOIL: An Analysis and Design System for Low Reynolds Number Airfoils," Conference on Low Reynolds Number Airfoil Aerodynamics, University of Notre Dame, June 1989.

10. FUN3D Manual: 13.1, Robert T. Biedron, Jan-Renee Carlson, Joseph M. Derlaga, Peter A. Gnoffo, Dana P. Hammond, William T. Jones, Bil Kleb, Elizabeth M. Lee-Rausch, Eric J. Nielsen, Michael A. Park, Christopher L. Rumsey, James L. Thomas, and William A. Wood, NASA-TM-2016-219580, 2016.